**Astronomy
&
Astrophysics**

LETTER TO THE EDITOR

First direct detection of an exoplanet by optical interferometry

Astrometry and *K*-band spectroscopy of HR 8799 e[*,**]

GRAVITY Collaboration: S. Lacour[1,2], M. Nowak[1], J. Wang[20,***], O. Pfuhl[2], F. Eisenhauer[2], R. Abuter[8],
A. Amorim[6,14], N. Anugu[7,22], M. Benisty[5], J. P. Berger[5], H. Beust[5], N. Blind[10], M. Bonnefoy[5], H. Bonnet[8],
P. Bourget[9], W. Brandner[3], A. Buron[2], C. Collin[1], B. Charnay[1], F. Chapron[1], Y. Clénet[1], V. Coudé du Foresto[1],
P. T. de Zeeuw[2,12], C. Deen[2], R. Dembet[1], J. Dexter[2], G. Duvert[5], A. Eckart[4,11], N. M. Förster Schreiber[2], P. Fédou[1],
P. Garcia[7,9,14], R. Garcia Lopez[15,3], F. Gao[2], E. Gendron[1], R. Genzel[2,13], S. Gillessen[2], P. Gordo[6,14],
A. Greenbaum[16], M. Habibi[2], X. Haubois[9], F. Haußmann[2], Th. Henning[3], S. Hippler[3], M. Horrobin[4], Z. Hubert[1],
A. Jimenez Rosales[2], L. Jocou[5], S. Kendrew[17,3], P. Kervella[1], J. Kolb[9], A.-M. Lagrange[5], V. Lapeyrère[1],
J.-B. Le Bouquin[5], P. Léna[1], M. Lippa[2], R. Lenzen[3], A.-L. Maire[19,3], P. Mollière[12], T. Ott[2], T. Paumard[1],
K. Perraut[5], G. Perrin[1], L. Pueyo[18], S. Rabien[2], A. Ramírez[9], C. Rau[2], G. Rodríguez-Coira[1], G. Rousset[1],
J. Sanchez-Bermudez[21,3], S. Scheithauer[3], N. Schuhler[9], O. Straub[1,2], C. Straubmeier[4], E. Sturm[2], L. J. Tacconi[2],
F. Vincent[1], E. F. van Dishoeck[2,12], S. von Fellenberg[2], I. Wank[4], I. Waisberg[2], F. Widmann[2], E. Wieprecht[2],
M. Wiest[4], E. Wiezorrek[2], J. Woillez[8], S. Yazici[2,4], D. Ziegler[1], and G. Zins[9]

(Affiliations can be found after the references)

ABSTRACT

Aims. To date, infrared interferometry at best achieved contrast ratios of a few times 10^{-4} on bright targets. GRAVITY, with its dual-field mode, is now capable of high contrast observations, enabling the direct observation of exoplanets. We demonstrate the technique on HR 8799, a young planetary system composed of four known giant exoplanets.
Methods. We used the GRAVITY fringe tracker to lock the fringes on the central star, and integrated off-axis on the HR 8799 e planet situated at 390 mas from the star. Data reduction included post-processing to remove the flux leaking from the central star and to extract the coherent flux of the planet. The inferred K band spectrum of the planet has a spectral resolution of 500. We also derive the astrometric position of the planet relative to the star with a precision on the order of 100 µas.
Results. The GRAVITY astrometric measurement disfavors perfectly coplanar stable orbital solutions. A small adjustment of a few degrees to the orbital inclination of HR 8799 e can resolve the tension, implying that the orbits are close to, but not strictly coplanar. The spectrum, with a signal-to-noise ratio of ≈ 5 per spectral channel, is compatible with a late-type L brown dwarf. Using Exo-REM synthetic spectra, we derive a temperature of 1150 ± 50 K and a surface gravity of $10^{4.3 \pm 0.3}$ cm s^2. This corresponds to a radius of $1.17^{+0.13}_{-0.11} R_{\rm Jup}$ and a mass of $10^{+7}_{-4} M_{\rm Jup}$, which is an independent confirmation of mass estimates from evolutionary models. Our results demonstrate the power of interferometry for the direct detection and spectroscopic study of exoplanets at close angular separations from their stars.

Key words. stars: individual: HR 8799 – planets and satellites: atmospheres – planet-star interactions – techniques: interferometric

1. Introduction

Obtaining accurate orbits, masses, and atmospheric spectra of directly imaged planets is key to determining their natures and, ultimately, their formation histories. Here we demonstrate the power of a new technique, using optical interferometry, to obtain this information for an exoplanet as close as 390 mas to its parent star.

Because they are better known, the spectra of brown dwarfs (BD) are often used as references to classify the young exoplanet atmospheres. More precisely, the L-T transition is an important observable for understanding the evolution of atmospheres as a function of temperature. At lower temperatures (<1200 K), opacity changes due to the transition of CO to methane in chemical equilibrium, and the likely disappearance of silicate and iron clouds under the photosphere, makes the spectral appearance of T-type BDs bluer. On the contrary, young giant exoplanets of temperature ≈ 1000 K still have redder near-infrared colors typical of late-L BDs. This is explained by the relatively low surface gravity ($g \leq 10^4$ cm s^2), and hence larger scale heights, in planetary atmospheres. However, the exact cause (cloud properties and/or vertical chemical mixing) is not properly understood (Allard et al. 2012). Once the problem of cloud formation and chemical processes are solved (Helling et al. 2014; Moses et al. 2016), the determination of the molecular composition of exoplanet atmospheres will become a crucial tool toward understanding the formation process of planets: the
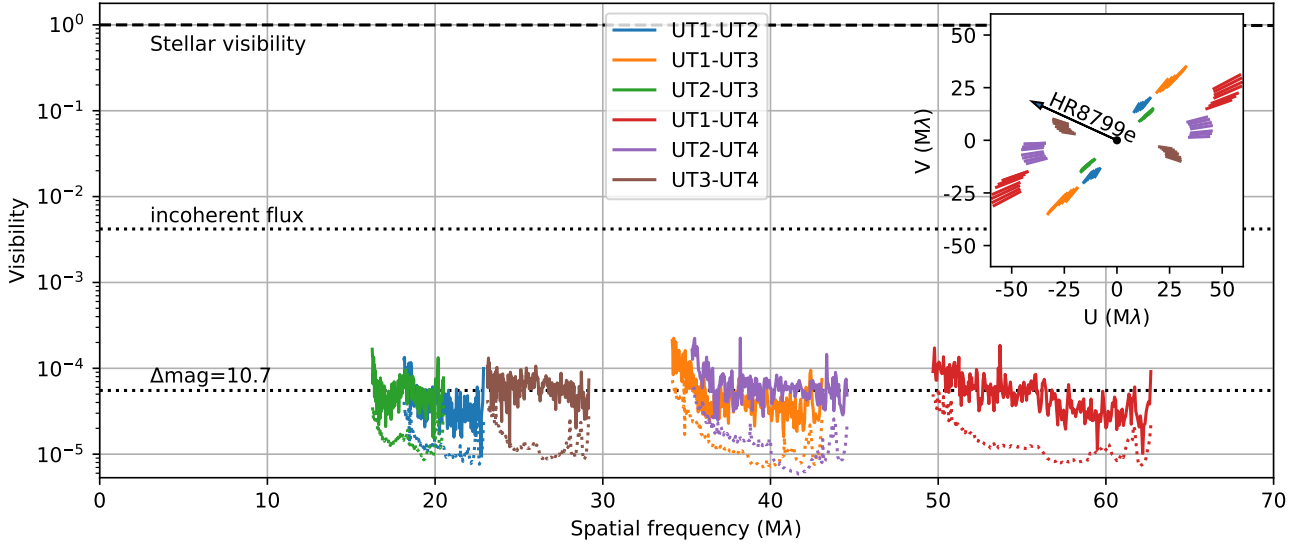

Fig. 1. Colored lines are HR 8799 e visibilities $|V_{planet}|$, as defined by Eq. (1), obtained from the ratio between the coherent flux observed on the planet and on the star. The underlying dotted colored lines correspond to the errors estimated by the pipeline. The theoretical stellar visibility corresponds to the black dashed line (uniform disk of diameter 0.342 mas). The upper horizontal dotted black line corresponds to the observed incoherent flux (stellar flux leaking in the planet's field). The lower horizontal dotted black line corresponds to the theoretical visibility of a planet 10.7 mag fainter than the star. Right inset: coverage of the spatial frequency plane, east is to the right. The arrow indicates the direction of the planet situated to the northwest of the star.

atomic ratio or even isotope ratio will change depending on the conditions of formation. For example, the C-to-O ratio in the gas of a protoplanetary disk is predicted to increase outwards past the H_2O (≈ 140 K), CO_2 (≈ 50 K), or even CO (≈ 20 K) ice-lines (Öberg et al. 2011): C/O in the planet atmosphere should therefore change depending on where in a disk planets form and how much gas and how many planetesimals they accrete (Mordasini et al. 2016). Similarly, the D-to-H ratio in planets can be linked to the accretion of icy bodies (Feuchtgruber et al. 2013) and can be seen in molecular absorption spectra (Mollière & Snellen 2019).

The study of cloud properties and composition requires spectral information, which can currently only be obtained by two means: transit spectroscopy or thermal emission spectroscopy. Transit spectroscopy is best for characterizing planets in close orbit around the host star, with puffy (inflated) irradiated atmospheres (Crossfield 2015, and references herein). Thermal emission spectroscopy is more adapted to young, self-luminous planets in orbits with a semimajor axis of a few tens of AU around the host star. Young planets are warm as they still possess excess entropy tracing back to the formation process (e.g., Marleau & Cumming 2014). The difficulty with emission spectroscopy is that a planet's signal is contaminated by stellar photons, which vary in time with changing observing conditions, resulting in a spatially and spectrally varying speckle pattern. One of the solutions for emission spectroscopy is to go to space to benefit from a stable point spread function. Another is to use high contrast and high angular resolution observations on 8 m to 10 m class telescopes from the ground, and to deconvolve the image to remove the speckles by using spectro-spatial correlations. This is typically done using integral field spectroscopy and techniques like spectral differential imaging (Rameau et al. 2015) or angular differential imaging (Marois et al. 2006).

With the technique presented in this paper, we go one step further by using the resolving power of the ≈ 100 m baselines offered by optical interferometry to distinguish between the coherent flux originating from the star and from the planet. In

Sect. 2 we present the GRAVITY observation of HR 8799 e and the data reduction. HR 8799 is a bright ($K = 5.24$ mag), nearby ($d = 39.4 \pm 0.1$ pc) A5 star. We know that at least four planets are orbiting the star (the first three discovered by Marois et al. 2008). In Sect. 3 we present a new astrometric measurement of the fourth planet ($K = 15.9$ mag), discovered in 2010 by Marois et al. (2010) at 368 ± 9 mas from its host star. The youth of the star (≈ 30 Myr, member of the Columba Association Malo et al. 2013), implies that the planet is still warm from its initial gravitational energy. In Sect. 4 we use the K-band spectra and photometry to constrain its spectral type, temperature, and radius. Finally, in Sect. 5, we summarize our results and briefly address the prospects of the interferometric technique.

2. Observations and data reduction

The observations were obtained with the VLTI using the four 8 m Unit Telescopes and the GRAVITY instrument (Eisenhauer et al. 2011; Gravity Collaboration 2017) on 28 August 2018. GRAVITY can observe two objects located in the VLTI field of view by simultaneously injecting, at each telescope coudé focus, the light of each object into a separate single-mode fiber. The two fibers have an effective field of view equal to ≈ 60 mas, the K-band diffraction limit of a single telescope (Pfuhl et al. 2014). Each object is thus interferometrically observed separately, but an ultraprecise laser telemetry constantly monitors the differential optical path between the two objects. The first fiber of GRAVITY was placed on the star for fringe tracking (Lacour et al. 2019) and phase referencing. The second fiber was centered sequentially on the planet and on the star, situated at ≈ 390 mas from each other. This second fiber fed the science spectrometer configured at medium resolution ($R = 500$). Observations of the star were used to calibrate the observation of the planet. Because of the faintness of the planet, a detector integration time (DIT) of 100 s was required. As the star is more than 10 mag brighter than the planet in K band, a DIT of 1 s was sufficient for the

Table 1. Observing log (data taken on 2018-Aug-28).

Target	UT Time	DIT	NDIT	Seeing	τ_0	Airmass	par. angle
Planet	04:33:59	100 s	10	0.8″	4.9 ms	1.48	−164.3°
Star	04:51:27	1 s	50	0.5″	7.1 ms	1.45	−169.6°
Sky	04:52:56	1 s	50	0.5″	6.7 ms	1.45	−170.0°
Planet	04:54:35	100 s	10	0.6″	6.2 ms	1.45	−170.6°
Planet	05:11:55	100 s	10	0.6″	6.2 ms	1.44	−176.0°
Sky	05:29:27	100 s	10	0.4″	8.5 ms	1.44	178.5°
Planet	05:46:56	100 s	10	0.5″	6.3 ms	1.44	172.9°
Planet	06:07:13	100 s	10	0.6″	5.6 ms	1.47	166.7°
Star	06:24:42	1 s	50	0.8″	4.2 ms	1.50	161.5°
Sky	06:26:10	1 s	50	0.8″	3.9 ms	1.50	161.1°
Planet	06:28:04	100 s	10	0.7″	4.9 ms	1.50	160.5°
Planet	06:45:25	100 s	10	0.7″	6.2 ms	1.55	155.7°
Sky	07:04:02	100 s	10	1.0″	3.6 ms	1.62	150.9°

Notes. τ_0 is the coherence time in the visual (500 nm); par. angle is the parallactic angle.

science channel observations of the star. Seeing conditions were average to good. The log of the observations is presented in Table 1, where exposures on the planet are shown along the sky and stellar calibration exposures.

The frequency plane and the amplitude of the planet's visibilities are presented in Fig. 1. The colored dotted lines below the visibilities are the errors estimated by the pipeline. The mean S/N per spectral channel is ≈5. The detailed data reduction procedure will be presented by Nowak et al. (in prep.). The main steps are as follows:

1. Extraction of the coherent flux (the VISDATA) for individual files using the ESO GRAVITY pipeline[1];
2. Derivation of the position of the planet with respect to the star by fitting the coherent flux with models of the coherent flux from the star and from the planet;
3. Removal of the coherent flux of stellar origin by linear decomposition on the models of step 2. This step assumes the position of the planet from step 2;
4. Normalization in phase and amplitude of the remaining coherent flux by the coherent flux observed on the star multiplied by the theoretical visibility function of the star. This gives the complex visibility of the planet

$$V_{\text{planet}} = \frac{\text{VISDATA}_{\text{planet}}}{\text{VISDATA}^*_{\text{star}}} \times \frac{2J_1(\pi\theta_{\text{star}}u)}{\pi\theta_{\text{star}}u}, \quad (1)$$

where J_1 is a Bessel function of the first kind, of order 1; θ_{star} is the stellar diameter; and u is the spatial frequency in rad^{-1}. The amplitude of V_{planet} is plotted as solid curves in Fig. 1;

5. Retrieval of the spectrum of the planet by assuming a diameter for the planet and a synthetic stellar spectrum:

$$F_{\text{planet}} = \frac{|V_{\text{planet}}|F_{\text{star}}}{2J_1(\pi\theta_{\text{planet}}u)/\pi\theta_{\text{planet}}u}. \quad (2)$$

The stellar diameter is assumed to be $\theta_{\text{star}} = 0.342 \pm 0.008$ mas (Baines et al. 2012) and is plotted as the black dashed line in Fig. 1. The planet diameter is assumed to be negligible at the resolution of the interferometer. For the star, we used a BT-NextGen model ($T = 7400$ K, [Fe/H] = −0.5, and log(g) = 4.0) from Hauschildt et al. (1999), scaled for a *K*-band flux of 3.191×10^{-12} W m^{-2} μm^{-1}.

Table 2. Astrometry on HR 8799 e.

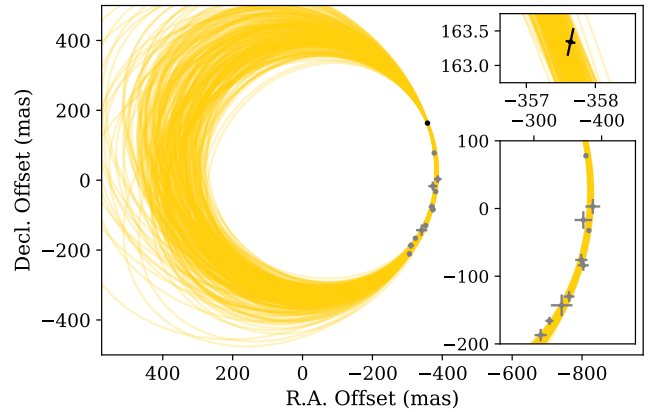| MJD	ΔRA (mas)	ΔDec (mas)	Covariance (mas^2)
58358.190	−357.63	163.59	
58358.205	−357.68	163.63	
58358.217	−357.54	163.05	
58358.241	−357.58	163.28	
58358.255	−357.61	163.12	
58358.269	−357.62	163.22	
58358.282	−357.80	163.41	
Global	−357.64 ± 0.07	163.34 ± 0.18	−0.00668

Fig. 2. Keplerian orbit fit of HR 8799 e. The black point is the GRAVITY measurement, and the gray points are from previous astrometry (Konopacky et al. 2016; Wang et al. 2018a). The yellow lines are 250 random draws from the posterior. The orbit determination is currently limited by the mas-level astrometry of the previous epochs (top inset). Image magnified by ~200x to display the uncertainties in the GRAVITY astrometry. The plotted error bars are rotated to be aligned with the principal axes of the error ellipse. Bottom inset: image magnified by ~2x to display the uncertainties in the previous measurements.

The upper dotted black line corresponds to the average residual flux from the star entering the science spectrometer. The lower dotted black line corresponds to the theoretical flux of an unresolved source with a 10.7 difference in magnitude.

3. Relative astrometry

In the same way as we can disentangle the complex coherent energy from the star and the planet, it is also possible to fit the wavelength dependence of the phase, which is tantamount to measuring a separation. Each fit, for each baseline, gives a χ^2 minimum for an optimal optical path difference (OPD). This OPD corresponds to an angular separation projected in the direction of the baseline vector. Several of these optimal OPDs are necessary to derive a position. By combining all the baselines together, we can use each exposure file separately, giving the seven optimal positions listed in Table 2. The global minimum is at ΔRA = −357.64 ± 0.07 mas and ΔDec = 163.34 ± 0.18 mas with highly elliptical uncertainty (covariance of −0.00668 mas^2). Along the longest baseline (position angle, PA = 78°) the 1σ uncertainty is 55 μas. Orthogonal to that baseline (PA = 168°) the uncertainty is 190 μas. The plate scale and true north error is negligible at that level (>50 μas) as the spatial frequencies are defined by the physical position of the telescopes. Atmospheric dispersion is also negligible. A detailed description of the error
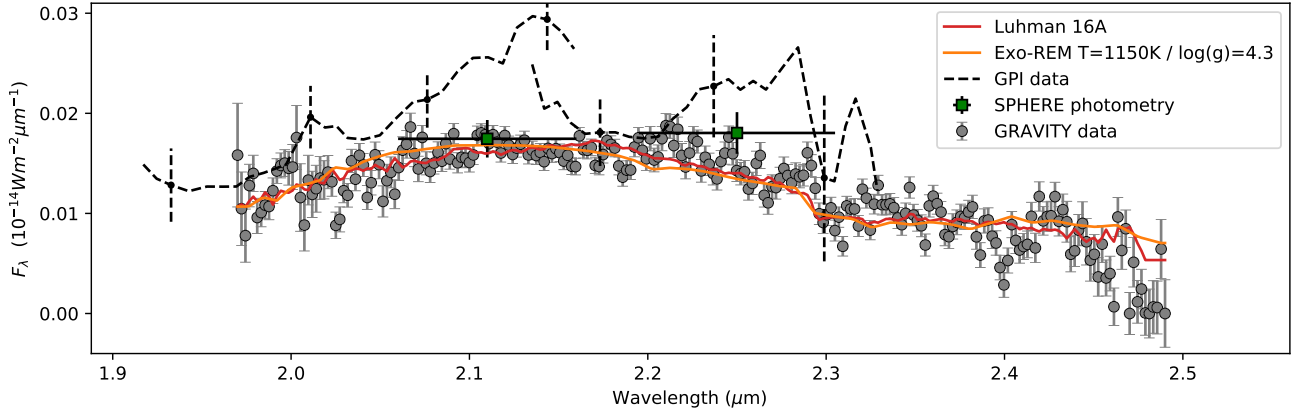
Fig. 3. GRAVITY K band spectrum of HR8799 e at spectral resolution 500 (gray points). The red curve is the X-SHOOTER spectrum of the brown dwarf Luhman 16 A from Lodieu et al. (2015), smoothed to the GRAVITY resolution. The reduced $\chi^2_{\rm red}$ is 2.4 (over 236° of freedom). The orange curve is the best fit of the Exo-REM models from Charnay et al. (2018). The reduced $\chi^2_{\rm red}$ is 2.7. The dashed curve is the K-band GPI spectrum from Greenbaum et al. (2018). The square dots are the SPHERE photometry from Zurlo et al. (2016).

terms of interferometric astrometry is presented in Lacour et al. (2014).

As this astrometry is an order of magnitude more precise than the best measurements made by direct imaging instruments (Wang et al. 2018a), we investigate the orbital constraints provided by this datapoint. We fit a single Keplerian orbit by combining this measurement with the astrometry reported in Konopacky et al. (2016) and Wang et al. (2018a). Given the assymetry in the GRAVITY measurement, we fit for the location of the planet at the GRAVITY epoch in a rotated frame that is aligned with the two principal axes of the error ellipse (top inset of Fig. 2). We use the parallel-tempered Markov chain Monte Carlo sampler (Foreman-Mackey et al. 2013; Vousden et al. 2016) in the orbit fitting code `orbitize` (Blunt et al. 2019) to estimate the orbital parameters and find a semimajor axis of $16.4^{+2.1}_{-1.1}$ AU, an eccentricity of 0.15 ± 0.08, and an inclination of $25° \pm 8°$. A single $100\,\mu$as precision point is able to significantly constrain the position of the planet at the epoch of observation, but the determination of the planet's velocity, acceleration, and orbital properties are still dominated by the mas-level uncertainties in the previous astrometry. We therefore defer a thorough dynamical study to a time when multi-epoch orbital monitoring of the planet with VLTI/GRAVITY has been obtained.

We can also compare the location of the planet measured by GRAVITY with the ΔRA $= -352.6^{+3.1}_{-2.6}$ mas and ΔDec $= -157.9 \pm 1.8$ mas predicted by the dynamically stable coplanar solutions from Wang et al. (2018a). The positions are inconsistent by 5 mas in both axes and none of the 9792 stable coplanar orbits are consistent with our measurement at the 3σ level. With this single astrometric point, we are therefore able to disfavor dynamically stable configurations in which the four planets are perfectly coplanar. Changing the inclination of HR 8799 e by $\approx -2°$ accounts for this 5 mas difference, and Wang et al. (2018a) did find 14 stable non-coplanar orbits with mutual inclinations of less 8° out of 20 million trials. We note that given the uncertainties in the orbital planes of the other three planets, we cannot pinpoint the mutual inclinations of the planets in this simple analysis. Continued monitoring of the orbit with GRAVITY can further constrain the planet's orbital elements, allowing a search for dynamically stable non-coplanar orbital solutions to be computationally tractable and providing more accurate constraints on the masses of the multiple planets.
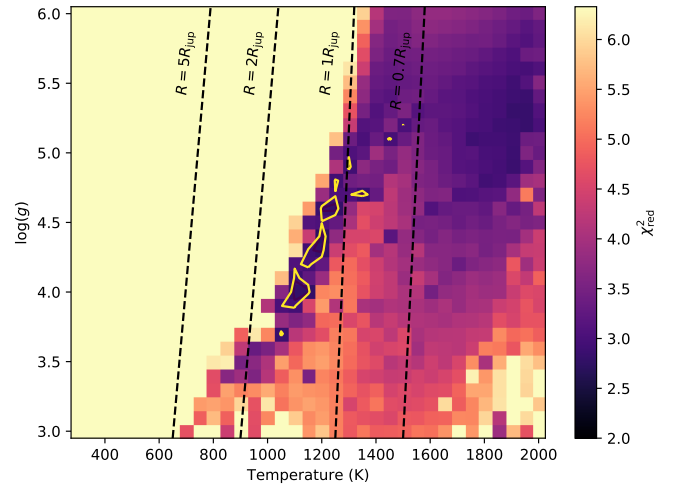

Fig. 4. Reduced χ^2 as a function of effective temperature and surface gravity from a grid of Exo-REM models (Charnay et al. 2018). The yellow contours correspond to the 5σ error, indicating a valley of possible temperatures between 1100 and 1200 K. The vertical lines correspond to the planet's radius from the model K-band luminosity assuming a distance of 39.4 pc.

4. Atmosphere of HR 8799 e

The GRAVITY spectrum of HR 8799 e was obtained by multiplying the visibility of the planet with the theoretical spectrum of the star. This is following Eq. (2) and assuming $\theta_{\rm planet} = 0$. The resulting spectrum is represented as the gray points in Fig. 3. The CO-band head at $2.29\,\mu$m is the most prominent feature. As already mentioned by Konopacky et al. (2013) and Wang et al. (2018b) for HR8799 c, no clear CH_4 absorption is seen, in agreement with a typical L-type BD spectrum. Using H and K band GPI spectra, Greenbaum et al. (2018) obtained a best fit with the spectrum of the brown dwarf WISE J1049-5319A (also called Luhman 16 A from Luhman 2013) of spectral type L7.5. The fit is equally good with the GRAVITY spectrum, and gives a reduced $\chi^2_{\rm red}$ of 2.4.

We fitted the catalog of BD spectra from the Montreal library (Gagné et al. 2015; Robert et al. 2016) to try to narrow down the spectral type from K-band spectroscopy only. With a reduced χ^2 of 2.4, the best fit indicates a spectral type close to L7 BD,

in agreement with Bonnefoy et al. (2016) and Greenbaum et al. (2018). A T-type BD spectrum is clearly ruled out. The reduced χ^2 increases to 3 for spectral types $\approx$L4, which is significant with $230°$ of freedom. Similarly, we fitted a grid of BT-Settl 2014 synthetic spectra (Baraffe et al. 2015) to derive a temperature and a surface density. The best fit was obtained for a temperature of 1400 K and a surface gravity of 10^4 cm s^2. This corresponds to a planetary radius of 0.8 $R_{\rm Jup}$.

This radius being incompatible with evolutionary models, we turned to the Exo-REM model (Baudino et al. 2015; Charnay et al. 2018). We found that values of 1150 ± 50 K and $\log(g) = 4.3 \pm 0.3$ (error bars 3σ) correctly reflect the spectrum in the *K* band (Fig. 4). According to the luminosity estimated by the model, it corresponds to a radius of $R = 1.17^{+0.13}_{-0.11} R_{\rm Jup}$. This gives a model-dependent estimate of the mass of HR 8799 e of $10^{+7}_{-4} M_{\rm Jup}$. Simulations with Exo-REM predict that the LT transition occurs at a lower effective temperature for exoplanets than for field brown dwarfs, due to effects of pressure on the formation of iron and silicate clouds. This trend is apparent in Fig. 4, where the LT transition corresponds to a sudden increase in χ^2 and occurs at an effective temperature just 100 K lower than our best fit.

5. Summary and conclusions

Interferometric astrometry, an order of magnitude more accurate than direct imaging, opens new possibilities to study the dynamics of planetary systems. With just a single data point from GRAVITY, we can strongly disfavor perfectly coplanar stable orbits for the HR 8799 planets. As the dynamics probe the masses, formation history, and the future system architecture, interferometric orbital monitoring at the 10–100μas level can significantly improve our understanding of directly imaged systems.

Based on the *K*-band spectrum, we confirm a spectral type ($\approx$L7), equivalent to a higher temperature BD. The discrepancy between spectral type ($T > 1400$ K; Schweitzer et al. 2002) and effective temperature derived from wide-band photometry ($T < 1200$ K) can be solved by using models taking the lower surface gravity into account. It is interesting to note that the GRAVITY *K*-band spectrum does constrain this low surface gravity, as shown by the residual map in Fig. 4. We determine a surface gravity compatible with a 10 $M_{\rm Jup}$ planet.

The interferometric technique brings unique possibilities to characterize exoplanets. With the technique described here, any planet with Kmag $\lessgtr$ 19, ΔKmag $\lessgtr$ 11, and separation $\gtrsim$100 mas is, in theory, observable with GRAVITY. The numbers are still to be refined, but it would mean that GRAVITY could observe most of the known imaged planets, and maybe in the near future planets detected by radial velocity. Furthermore, the good normalization of the continuum spectrum offers new ways to measure the column density of molecules without the need for smoothing and cross-correlation (e.g., Snellen et al. 2014; Konopacky et al. 2013). Finally, the idea that an interferometer can resolve the surface of exoplanets, giving radius and resolving clouds patchiness, is now becoming more plausible. However, it would require an interferometer with baselines on the order of 10 km. This could be a goal for ESO after ELT construction.

References

Allard, F., Homeier, D., Freytag, B., & Sharp, C. M. 2012, EAS Pub. Ser., 57, 3
Baines, E. K., White, R. J., Huber, D., et al. 2012, ApJ, 761, 57
Baraffe, I., Homeier, D., Allard, F., & Chabrier, G. 2015, A&A, 577, A42
Baudino, J.-L., Bézard, B., Boccaletti, A., et al. 2015, A&A, 582, A83
Blunt, S., Ngo, H., Wang, J., et al. 2019, Sblunt/Orbitize: Expand Default Orbit Plots (Zenodo)
Bonnefoy, M., Zurlo, A., Baudino, J. L., et al. 2016, A&A, 587, A58
Charnay, B., Bézard, B., Baudino, J.-L., et al. 2018, ApJ, 854, 172
Crossfield, I. J. M. 2015, PASP, 127, 941
Eisenhauer, F., Perrin, G., Brandner, W., et al. 2011, The Messenger, 143, 16
Feuchtgruber, H., Lellouch, E., Orton, G., et al. 2013, A&A, 551, A126
Foreman-Mackey, D., Hogg, D. W., Lang, D., & Goodman, J. 2013, PASP, 125, 306
Gagné, J., Faherty, J. K., Cruz, K. L., et al. 2015, ApJS, 219, 33
Gravity Collaboration (Abuter, R., et al.) 2017, A&A, 602, A94
Greenbaum, A. Z., Pueyo, L., Ruffio, J.-B., et al. 2018, AJ, 155, 226
Hauschildt, P. H., Allard, F., Ferguson, J., Baron, E., & Alexander, D. R. 1999, ApJ, 525, 871
Helling, C., Woitke, P., Rimmer, P. B., et al. 2014, Life, 4, 142
Konopacky, Q. M., Barman, T. S., Macintosh, B. A., & Marois, C. 2013, Science, 339, 1398
Konopacky, Q. M., Marois, C., Macintosh, B. A., et al. 2016, AJ, 152, 28
Lacour, S., Eisenhauer, F., Gillessen, S., et al. 2014, A&A, 567, A75
Lacour, S., Dembet, R., Abuter, R., et al. 2019, A&A, accepted [arXiv:1901.03202]
Lodieu, N., Osorio, M. R. Z., Rebolo, R., et al. 2015, A&A, 581, A73
Luhman, K. L. 2013, ApJ, 767, L1
Malo, L., Doyon, R., Lafrenière, D., et al. 2013, ApJ, 762, 88
Marleau, G.-D., & Cumming, A. 2014, MNRAS, 437, 1378
Marois, C., Lafreniere, D., Doyon, R., Macintosh, B., & Nadeau, D. 2006, ApJ, 641, 556
Marois, C., Macintosh, B., Barman, T., et al. 2008, Science, 322, 1348
Marois, C., Zuckerman, B., Konopacky, Q. M., Macintosh, B., & Barman, T. 2010, Nature, 468, 1080
Mollière, P., & Snellen, I. A. G. 2019, A&A, 622, A139
Mordasini, C., van Boekel, R., Mollière, P., Henning, T., & Benneke, B. 2016, ApJ, 832, 41
Moses, J. I., Marley, M. S., Zahnle, K., et al. 2016, ApJ, 829, 66
Öberg, K. I., Murray-Clay, R., & Bergin, E. A. 2011, ApJ, 743, L16
Pfuhl, O., Haug, M., Eisenhauer, F., et al. 2014, Optical and Infrared Interferometry IV, 9146, 914623
Rameau, J., Chauvin, G., Lagrange, A. M., et al. 2015, A&A, 581, A80
Robert, J., Gagné, J., Artigau, E., et al. 2016, ApJ, 830, 144
Schweitzer, A., Gizis, J. E., Hauschildt, P. H., et al. 2002, ApJ, 566, 435
Snellen, I. A. G., Brandl, B. R., de Kok, R. J., et al. 2014, Nature, 509, 63
Vousden, W. D., Farr, W. M., & Mandel, I. 2016, MNRAS, 455, 1919
Wang, J. J., Graham, J. R., Dawson, R., et al 2018a, AJ, 156, 192
Wang, J., Mawet, D., Fortney, J. J., et al. 2018b, AJ, 156, 272
Zurlo, A., Vigan, A., Galicher, R., et al. 2016, A&A, 587, A57

1 LESIA, Observatoire de Paris, Université PSL, CNRS, Sorbonne Université, Univ. Paris Diderot, Sorbonne Paris Cité, 5 place Jules Janssen, 92195 Meudon, France
e-mail: sylvestre.lacour@obspm.fr, mathias.nowak@obspm.fr
2 Max Planck Institute for extraterrestrial Physics, Giessenbachstraße 1, 85748 Garching, Germany
3 Max Planck Institute for Astronomy, Königstuhl 17, 69117 Heidelberg, Germany
4 1st Institute of Physics, University of Cologne, Zülpicher Straße 77, 50937 Cologne, Germany
5 Univ. Grenoble Alpes, CNRS, IPAG, 38000 Grenoble, France
6 Universidade de Lisboa – Faculdade de Ciências, Campo Grande, 1749-016 Lisboa, Portugal

[7] Faculdade de Engenharia, Universidade do Porto, rua Dr. Roberto Frias, 4200-465 Porto, Portugal

[8] European Southern Observatory, Karl-Schwarzschild-Straße 2, 85748 Garching, Germany

[9] European Southern Observatory, Casilla 19001, Santiago 19, Chile

[10] Observatoire de Genève, Université de Genève, 51 Ch. des Maillettes, 1290 Versoix, Switzerland

[11] Max Planck Institute for Radio Astronomy, Auf dem Hügel 69, 53121 Bonn, Germany

[12] Sterrewacht Leiden, Leiden University, Postbus 9513, 2300 RA Leiden, The Netherlands

[13] Departments of Physics and Astronomy, Le Conte Hall, University of California, Berkeley, CA 94720, USA

[14] CENTRA – Centro de Astrofísica e Gravitação, IST, Universidade de Lisboa, 1049-001 Lisboa, Portugal

[15] Dublin Institute for Advanced Studies, 31 Fitzwilliam Place, Dublin 2, Ireland

[16] Department of Astronomy, University of Michigan, Ann Arbor, MI 48109, USA

[17] European Space Agency, Space Telescope Science Institute, 3700 San Martin Drive, Baltimore, MD 21218, USA

[18] Space Telescope Science Institute, Baltimore, MD 21218, USA

[19] STAR Institute, Université de Liège, Allée du Six Août 19c, 4000 Liège, Belgium

[20] Department of Astronomy, California Institute of Technology, Pasadena, CA 91125, USA

[21] Instituto de Astronomía, Universidad Nacional Autónoma de México, Apdo. Postal 70264, Ciudad de México 04510, Mexico

[22] School of Physics, Astrophysics Group, University of Exeter, Stocker Road, Exeter EX4 4QL, UK